Trends and uncertainties in thermal calibration of AVHRR radiometers onboard NOAA-9 to NOAA-16

Alexander P. Trishchenko,[1] Gunar Fedosejevs,[1] Zhanqing Li,[2] and Josef Cihlar[1]

[1] Satellite measurements from the infrared (IR) channels of the Advanced Very High Resolution Radiometer (AVHRR)/NOAA have been used to derive many important atmospheric, cloud, and surface parameters for weather prediction, climate modelling, and a variety of environmental studies. Calibration accuracy of the satellite data directly affects accuracies of the derived parameters. So far, very limited attention has been given to the calibration uncertainties of the IR channels. In this study, we analyzed the calibration data of AVHRR radiometers onboard polar orbiting satellites NOAA-9 to NOAA-16. We utilized Global Area Coverage (GAC) data, approximately one orbit per month throughout the lifetime of the instruments, available from the NOAA Satellite Active Archive (SAA). AVHRR IR channels 3B, 4, and 5 are calibrated in-flight. Calibration coefficients are derived from measurements of radiance emitted from an internal calibration target (ICT) and deep-space (SP). The overall budget of uncertainties has been evaluated using an in-flight calibration system that includes four thermal platinum resistance thermometers (PRTs) to monitor the ICT temperature. The measurement noise (NEΔT) was found to vary from 0.03 K to 0.3 K at 300 K depending on the channel and radiometer, and it increases significantly as temperature decreases. Systematic degradation of the radiometric sensitivity of the IR detectors was observed during the lifetime of a radiometer, although the annual rate of degradation is rather small (typically below 1% per year). A significant correlation between the calibration gain and temperature of a radiometer is often observed. The degradation of a sensor's radiometric sensitivity reduces the radiometric resolution of the AVHRR measurements and expands the upper limit of the measured brightness temperature. PRT measurements are subject to significant orbital variation (up to 7 K) and inconsistency for some AVHRR radiometers. The inconsistency was especially large for the AVHRR onboard NOAA-12 (up to 4 K) and NOAA-14 (up to 3 K), but it is less than 0.5 K for NOAA-15 and -16. The inconsistency may signify the presence of a thermal gradient across the ICT. Some systematic differences between PRT measurements may also indicate inaccurate characterization of the PRT sensors, for example for AVHRR/NOAA-11 and -14. The impact of the varying thermal state of the AVHRR environment on the accuracy of AVHRR in-flight thermal calibration was assessed. We found this impact to be significant (up to 0.5 K and more), and proposed a physical model to explain it. We recommend this model for AVHRR operational in-flight calibration, especially during solar radiative contamination events. Estimates of the PRT thermal response time constant were derived and found to vary between 0.5 and 1.5 min among AVHRR radiometers. Overall, we found somewhat higher uncertainties in AVHRR thermal measurements than were assumed previously. *INDEX TERMS:* 1640 Global Change: Remote sensing; 1694 Global Change: Instruments and techniques; 3360 Meteorology and Atmospheric Dynamics: Remote sensing; 3394 Meteorology and Atmospheric Dynamics: Instruments and techniques

Citation: Trischenko, A. P., G. Fedosejevs, Z. Li, and J. Cihlar, Trends and uncertainties in thermal calibration of AVHRR radiometers onboard NOAA-9 to -16, *J. Geophys. Res.*, *107*(D24), 4778, doi:10.1029/2002JD002353, 2002.

[1]Canada Centre for Remote Sensing, Natural Resources Canada, Ottawa, Ontario, Canada.

[2]Earth System Science Interdisciplinary Center, University of Maryland, College Park, Maryland, USA.

1. Introduction

[2] The Advanced Very High Resolution Radiometer (AVHRR) onboard the National Oceanic and Atmospheric Administration's (NOAA) polar orbiting satellites is perhaps the most widely used sensor for operational and long-term monitoring of global atmospheric, oceanic and terrestrial

environments from space [*Cracknell*, 1997; *Rao et al.*, 1990; *Cihlar et al.*, 2002]. Many important parameters assimilated in numerical weather prediction models, employed in climate and other studies are extracted from the AVHRR thermal data. As such, thorough understanding of uncertainties in the thermal calibration data is of critical importance. So far, however, this issue has been poorly addressed [*Kidwell*, 1998].

[3] The first AVHRR models launched on board Tiros-N, NOAA-6, -8, -10 had four spectral channels. The second model known as AVHRR/2 was deployed on NOAA-7, -9, -11, -12, -14. The AVHRR/2 radiometers had 5 spectral channels: (1) visible $0.55-0.68$ μm, (2) near-infrared (NIR) channel $0.725-1.10$ μm, (3) shortwave infrared (channel 3B SWIR) $3.55-3.93$ μm, (4) thermal infrared (IR) $10.3-11.3$ μm, and (5) thermal infrared $11.5-12.5$ μm. New AVHRR/3 instruments onboard NOAA-15 and -16 have an additional channel 3A in the $1.585-1.635$ μm spectral region. Channels 3A and 3B operate interchangeably during the day (3A) and night (3B), respectively.

[4] Data from the AVHRR visible and NIR channels have been used to determine different land surface parameters such as surface reflectance [*Trishchenko et al.*, 2002], land cover types [*Cihlar*, 2000], normalised difference vegetation index (NDVI) [*Kidwell*, 1990] and absorbed photosynthetically active radiation (APAR) [*Li et al.*, 1997], and to retrieve aerosol optical depth [*Ignatov and Stowe*, 2002a, 2002b; *Stowe et al.*, 1997], among other parameters. One of the most important applications of AVHRR data from thermal channels 3B, 4 and 5 is estimation of the global sea surface temperature (SST) [*Reynolds and Smith*, 1993]. The thermal channels have also been used to retrieve cloud cover information [*Rossow*, 1989; *Trishchenko et al.*, 2001], land surface temperature, and thermal emissivity [*Qin and Karnieli*, 1999]. Forest fire detection and monitoring is also a very important application of AVHRR thermal data [*Li et al.*, 2001]. Global climate monitoring and change detection require SST and land surface temperatures with a high accuracy. The generally accepted requirement is ±0.1 K [*Kidwell*, 1998; *Vazquez and Sumagaysay*, 2001].

[5] Unlike the short-wave channels (1, 2, and 3A) that are not calibrated onboard, the thermal channels (3B, 4, and 5) are calibrated in-flight using measurements of the internal calibration target (ICT) and deep-space (SP) [*Cracknell*, 1997; *Kidwell*, 1998]. The thermal state of the ICT target is monitored by four platinum resistance thermistors (PRTs). Providing that the monitoring of the ICT temperature is accurate, the measurement error is limited by the magnitude of the noise equivalent delta temperature (NEΔT) for each thermal channel. Other factors, such as nonblackness of the ICT, that is, departure of its emissivity from unity, and reflections from surrounding elements contribute only about 10% of the total uncertainty [*Weinreb et al.*, 1990]. Usually, this uncertainty is estimated during preflight tests under laboratory conditions. Some information about the accuracy achieved during preflight ground IR calibration is available [*Brown et al.*, 1985, 1993; *Kidwell*, 1998; *Walton et al.*, 1998; *Sullivan*, 1999]. However, the accuracy of AVHRR operational IR measurements is not well characterized. We addressed this issue by conducting an analysis of NEΔT throughout the lifetime of AVHRRs from NOAA-9

to NOAA-16 (except AVHRR/NOAA-10 which was an AVHRR/1 type radiometer) based on Global Area Coverage (GAC) data available from the NOAA Satellite Active Archive (SAA).

[6] As we show below, the critical issue is the accuracy of the ICT temperature monitoring because any uncertainty in the ICT temperature directly converts into an uncertainty in the pixel brightness temperature. Our analysis shows that each PRT sensor, depending on its spatial location on the ICT, responds differently to thermal forcing. This forcing is caused by changes in solar heating and radiative cooling, which in turn depend on solar illumination conditions along an orbit and the relative position between the Sun and orbital plane for a given time of the year. An analysis of the correlation between PRT temperatures reveals complex thermal processes within the ICT, which impact negatively on the accuracy of AVHRR thermal calibration.

[7] The paper is organised as follows. Section 2 outlines the general principles of thermal calibration of AVHRR radiometers. Section 3 analyses the NEΔT for each thermal channel. Section 4 presents an analysis of ICT temperature data. The solar contamination effect and its impact on the accuracy of thermal calibration are also addressed in this section, together with an application of a sensor response model and the derivation of the sensor's time response constant. In section 5, long-term trends in thermal channel calibration gains are examined. Section 6 concludes the paper.

2. The Principles of AVHRR Thermal Calibration

[8] The physical principles of AVHRR thermal calibration are described by *Kidwell* [1998], *Cracknell* [1997], and *Planet* [1988]. Some useful notations and formulae used throughout the paper are introduced here.

[9] We denote the spectral response function of channel i as $r_i(\lambda)$. The normalized spectral response functions for AVHRR NOAA-14 and -16 channels 3B, 4, and 5 are presented in Figure 1. In-flight calibration of the thermal channels is based on the measurements of radiation emitted by the ICT and by deep space. The ICT operates approximately at the temperature of the radiometer's internal environment, which varies usually between 286 K and 300 K. The thermal detectors are typically maintained at a temperature of 107 K by a radiant cooler subsystem [*Cracknell*, 1997].

[10] There are 10 samples of SP and ICT counts as measured by the radiometer in every AVHRR scan line. They represent a digitized output of the radiometer when the scanning mirror views the SP and the ICT targets. The average of the 10 samples is usually used for calibration. To make calibration less sensitive to noise effects, a more robust approach is recommended [*Trishchenko*, 2002].

[11] Four PRTs imbedded in the ICT are used to monitor its temperature. Three samples of digital counts from each PRT are added to the output data stream for each scan line (minor data frame). The samples from only one PRT are included in each minor data frame, creating a sequence of four data sets and followed by a null data set in the output data stream in high-resolution picture transmission (HRPT) data. Therefore, digital counts are available from each PRT once for every 5 minor frames (5/6 of a second). The PRT
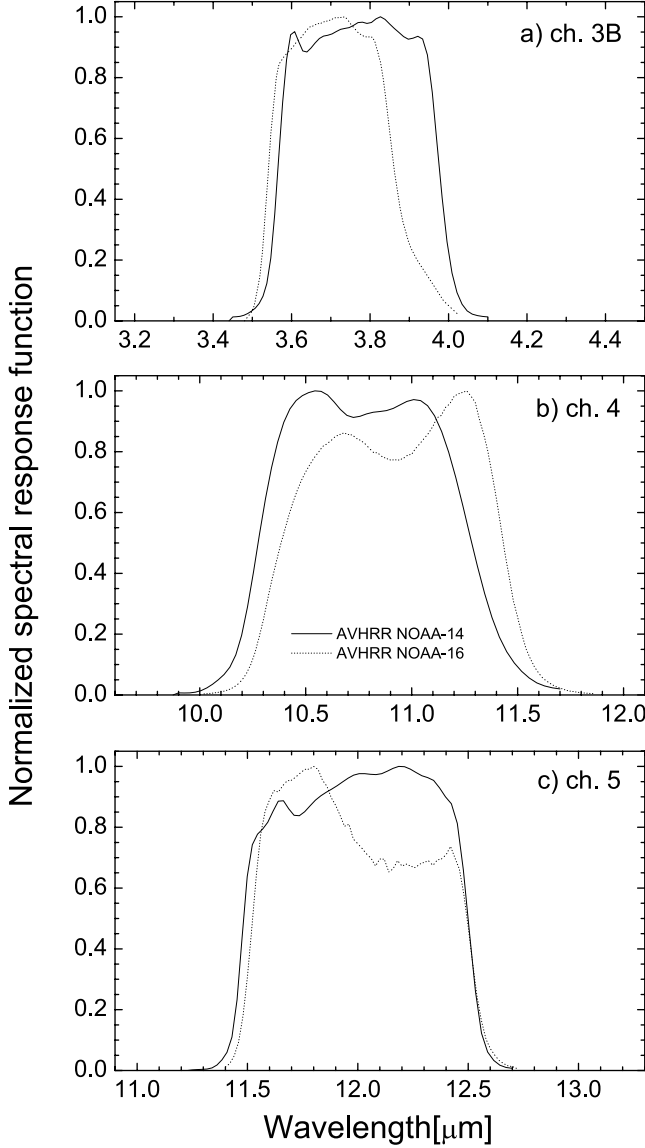
Figure 1. Spectral response functions for the AVHRR thermal channels (a) 3B, (b) 4, and (c) 5 onboard NOAA-14 (solid line) and NOAA-16 (dotted line).

data are used to uniquely determine the ICT temperature, T_{ICT}. To make it consistent with PRT observations, often 50 samples (5 scanlines) instead of 10 samples (1 scanline) are used to compute the average blackbody counts. The PRT sequence in GAC data differs from that of HRPT, since only every third scan line is included in the output data stream. The radiation R_{ICT}^i received by channel i detector from the ICT with unit emissivity (blackbody) is

$$R_{ICT}^i = \int_{\lambda_{min}}^{\lambda_{max}} B(\lambda, T_{ICT}) r_i(\lambda) d\lambda, \qquad (1)$$

where

$$B(\lambda, T) = \frac{c_1 \nu^3}{\exp\left(\frac{c_2 \nu}{T}\right) - 1}$$

is the Planck function,

$$c_1 = 1.1910659 \times 10^{-5} \text{ mW m}^{-2} \text{ sr}^{-1} \text{ cm}^4,$$

$$c_2 = 1.438833 \text{ cm} -°\text{K}.$$

The following expression is recommended for conversion of PRT counts into temperature for all 4 PRTs [Kidwell, 1998]:

$$T_{PRT} = a0 + a1*PRT + a2*PRT^2 + a3*PRT^3 + a4*PRT^4. \quad (2)$$

The ICT temperature, T_{ICT}, is derived as an average of the 4 PRT temperatures [Kidwell, 1998]:

$$T_{ICT} = 1/4(T_{PRT1} + T_{PRT2} + T_{PRT3} + T_{PRT4}). \qquad (3)$$

To compute radiometer channel calibration gains, $G^{(i)}$, and offsets, $I^{(i)}$, NOAA recommends using a small nonzero radiance value for the space target radiance, R_{SP}. These values are instrument- and channel-specific [Kidwell, 1998]. The calibration gain and offset values are determined from the following equations:

$$G^{(i)} = \frac{R_{ICT}^{(i)} - R_{SP}^{(i)}}{C_{ICT}^{(i)} - C_{SP}^{(i)}}, \qquad (4a)$$

$$I^{(i)} = R_{SP}^{(i)} - G^{(i)} \cdot C_{SP}^{(i)}, \qquad (4b)$$

where $C_{ICT}^{(i)}$ is the digital count for the internal calibration target and $C_{SP}^{(i)}$ is the digital count for the space target.

[12] The final step of calibration consists of a nonlinear correction that converts linear radiance R_{lin} into corrected radiance R for every pixel in channel i:

$$R^{(i)} = A^{(i)} \cdot R_{lin}^{(i)} + B^{(i)} \cdot \left(R_{lin}^{(i)}\right)^2 + D^{(i)}, \qquad (5)$$

where the linear radiance is

$$R_{lin}^{(i)} = G^{(i)} \cdot C_P^{(i)} + I^{(i)}. \qquad (6)$$

Coefficients $A^{(i)}$, $B^{(i)}$, and $D^{(i)}$ are known constants [Kidwell, 1998; Sullivan, 1999; Goodrum et al., 2000]. $C_P^{(i)}$ is the observed pixel response in counts. Nonlinear corrections for NOAA-9, -11 and -12 were implemented in data processing through look-up table approach instead of applying equation (5) [Kidwell, 1998].

[13] Although similar in principle, the thermal calibration procedure is slightly different for the KLM satellite series AVHRR/3. There is an effective blackbody temperature correction and an alternate nonlinear radiance correction equation as described in the NOAA KLM User's Guide http://www2.ncdc.noaa.gov/docs/intro.htm).

[14] Equation (1) assumes that all radiation observed by AVHRR thermal channel i is emitted by ICT with emissivity $\varepsilon = 1$, thus neglecting its departure from a perfect blackbody. The real situation is more complicated. A small departure of ε from 1 causes reflection of thermal radiation emitted by the AVHRR interior. As such, a more accurate expression would be

$$R_{ICT}^i = \int_{\lambda_{min}}^{\lambda_{max}} [\varepsilon(\lambda) B(\lambda, T_{ICT}) + (1 - \varepsilon(\lambda)) L(\lambda)] r_i(\lambda) d\lambda, \qquad (7)$$

Table 1. Statistics of Noise in the AVHRR Thermal Calibration Measurements[a]

Platform	Channel 3B		Channel 4		Channel 5		PRT
	SP	ICT	SP	ICT	SP	ICT	
NOAA-9	2.2−4.2	2.0−3.9	0.1−0.3	0.2−0.3	0.4−0.6	0.5−0.6	0.1−0.2
NOAA-11	1.6−2.1	1.5−2.3	0.1−0.2	0.1−0.2	0.4−0.5	0.4−0.5	0.1−0.2
NOAA-12	2.8−3.9	2.3−3.9	0.5−0.6	0.6−0.7	0.5−0.6	0.4−0.5	0.2−0.3
NOAA-14	2.5−3.2	2.3−3.1	0.2−0.5	0.2−0.3	0.4−0.5	0.4−0.5	0.3−0.4
NOAA-15	0.7−0.9	0.6−0.7	0.03−0.1	0.1−0.2	0.3−0.4	0.3−0.4	0.1−0.2
NOAA-16	0.4−0.5	0.4−0.5	0.5−0.6	0.4−0.5	0.7−0.8	0.6−0.7	<0.1

[a]Results are given in counts.

where $(1 - \varepsilon(\lambda))L(\lambda)$ is the total radiation reaching the ICT surface and reflected back toward the detector. When the ICT and its environment is in approximate thermal equilibrium, that is, $B(\lambda, T) \approx L(\lambda)$, then equation (7) is equal to equation (1).

3. Noise Equivalent Error NEΔT

[15] The NEΔT error can be derived from equations (1) to (5) assuming statistical independence and normal distribution of noise in the SP, ICT and PRT measurements.

[16] The expression for the uncertainty δR follows from equation (5):

$$\delta R = |A + 2BR_{lin}|\delta R_{lin} \approx \delta R_{lin}, \qquad (8)$$

since parameter B is small, and parameter A is close to 1. In equation (8) we omitted index "i" denoting the channel selection.

[17] Given the following expression for linear radiance:

$$R_{lin} = f\left(T_{ICT}, C_p, C_{ICT}, C_{sp}\right) = R_{sp} + \left(R_{ICT} - R_{sp}\right)\frac{C_p - C_{sp}}{C_{ICT} - C_{sp}} \quad (9)$$

and assuming statistical independence and normal distribution of δ-variations, the total uncertainty for linear radiance can be written as:

$$\delta R_{lin}$$
$$= \sqrt{\left(f'_{T_{ICT}}\right)^2 \delta T_{ICT}^2 + \left(f'_{C_{ICT}}\right)^2 \delta C_{ICT}^2 + \left(f'_{C_{sp}}\right)^2 \delta C_{sp}^2 + \left(f'_{C_p}\right)^2 \delta C_p^2}. \quad (10)$$

The δT_{ICT} error term in equation (10) is caused by noise in the PRT measurements. Assumption about statistical independence of δ-variations was confirmed by data analysis that showed very low level of correlation between ICT and SP noise at the level of 10^{-3} to 10^{-2}.

[18] To determine the noise equivalent error, we analyzed the standard deviations δC of ICT, SP, and PRT counts, for every scan line within a single GAC data file. Statistics for various AVHRR radiometers are presented in Table 1. Values in Table 1 are the average standard deviations for individual GAC data files. There are two values for each parameter to show typical range of variability; they were computed for GAC data files taken at the beginning and end of instrument operations to account for possible changes in instrument measurement properties throughout its lifetime.

[19] An example of standard deviations for AVHRR NOAA-16 on 5 February 2002 is shown in Figure 2. The left panels of Figure 2 contain SP counts and the right panels contain ICT counts. Panels from top to bottom are for channels 3B, 4, and 5. Switching to the channel 3A mode causes gaps in SP and ICT data for channel 3B in the two top panels (a−b). Channels 3A and 3B cannot operate at the same time.

[20] The instrument noise characteristics for SP and ICT observations are similar. These observations represent two extreme situations, corresponding to high and low radiance levels. We may assume that the noise level is also of the same magnitude for intermediate input signals. Therefore, the signal-to-noise ratio is greater for low pixel brightness temperature and smaller for higher brightness temperatures. Noise for channel 3 on AVHHR/2 varies within a range of 2 to 4 counts. The largest δC values for channel 3 were found for NOAA-9, -12, -14, and the smallest ones were for NOAA-11. Noise for channels 4 and 5 of AVHRR/2 are typically less than 0.5 count, except for NOAA-12 where it slightly exceeds this level. The magnitude of the noise in channel 3B of the AVHRR/3 model is much smaller and closer to values observed in channels 4 and 5. For NOAA-16, the noise in channel 5 exceeds the noise in channels 3B and 4.

[21] Uncertainties in the PRT counts are quite small, causing a negligible error in pixel brightness temperature (less than ±(0.01 to 0.02) K). We neglect this error by omitting the first term in equation (10). Note that the actual accuracy of ICT temperature measurements is not identical to the PRT noise error; this will be discussed further.

[22] Let us assume that the noise error for each type of calibration sample data and pixel count is the same, and denoted as δC. Equation (10) then becomes

$$\delta R_{lin} = \delta C\sqrt{\left(f'_{C_{ICT}}\right)^2 + \left(f'_{C_{sp}}\right)^2 + \left(f'_{C_p}\right)^2}. \qquad (11)$$

The derivatives are given by

$$f'_{C_{ICT}} = -G\frac{C_p - C_{SP}}{C_{ICT} - C_{SP}}; \quad f'_{C_{SP}} = G\frac{C_p - C_{ICT}}{C_{ICT} - C_{SP}}; \quad \text{and} \quad f'_{C_p} = G, \qquad (12)$$

where the gain G is determined by equation (4a). By introducing the variable

$$\varepsilon = \frac{C_p - C_{SP}}{C_{ICT} - C_{SP}}, \qquad (13)$$

we obtain the following expression for:

$$\delta R_{lin} = \sqrt{2}G(\delta C)\sqrt{1 - \varepsilon(1 - \varepsilon)}. \qquad (14)$$
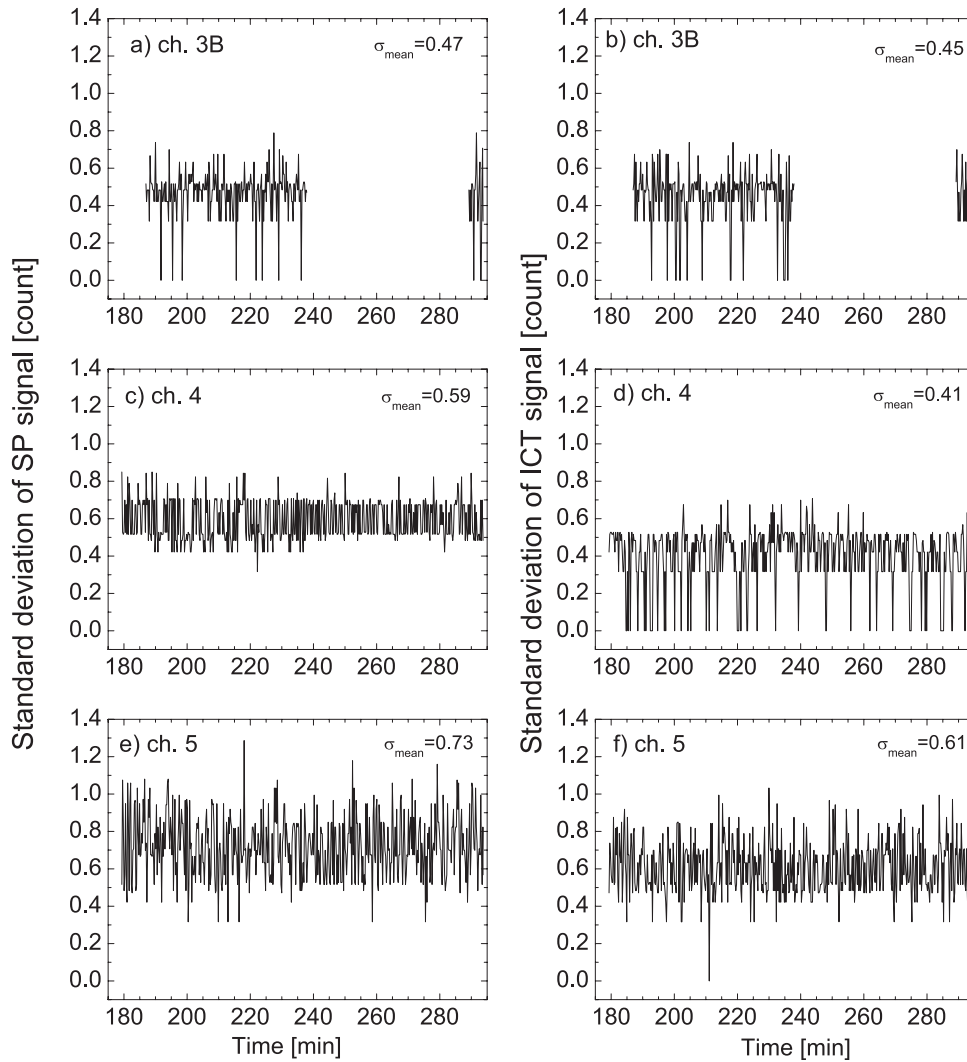
Figure 2. Standard deviations of SP counts for channels (a) 3B, (c) 4, and (e) 5 and ICT counts for channels (b) 3B, (d) 4, and (f) 5 for AVHRR NOAA-16. Data are for 5 February 2002. Gaps for channel 3B SP and ICT data correspond to the periods of channel 3A activation, when channel 3B is turned off.

[23] The NEΔT error computed according to equation (14) is presented in Figure 3. The panels from top to bottom are (a) for channel 3B, (b) channel 4, and (c) channel 5. The NEΔT error is shown as a function of pixel brightness temperature. In the calculations, we employed average numbers for the standard deviation δC shown in Table 1. Equation (14) also contains the calibration gain G. We used average values of gain over the instrument lifetime, presented in Table 2. The NEΔT for channels 4 and 5 is within the NOAA established threshold of 0.12 K at 300 K for all radiometers considered [*Kidwell*, 1998], although NEΔT for channel 5 of NOAA-16 is slightly larger ($\sim$0.13 K). The NEΔT for channel 3B is noticeably larger than the threshold (0.12 K) except for AVHRR NOAA-15 and -16. The NEΔT values for channel 3B may be as high as 0.3 K (NOAA-9 and -12). When the brightness temperature of a pixel decreases, the NEΔT error sharply increases; it may be as high as 0.2 K for channels 4 and 5 and 1−3 K at 250 K for channel 3B. The NEΔT errors for channels 4 and 5 of AVHRR NOAA-15 and -16 are larger than the NEΔT errors of channel 4 and 5 for all other considered radio-

meters. The corresponding NEΔT error for channel 3B of AVHRR NOAA-15 and -16 is the smallest among channel 3B NEΔT errors.

4. Accuracy of the ICT Temperature Monitoring

[24] Preflight testing and calibration is performed when the instrument is in a state of thermal equilibrium [*Walton et al.*, 1998]. In the case of in-flight operation, the radiometer temperature experiences periodic oscillations caused by the satellite moving in and out of sunlight during an orbit. It is generally believed that the AVHRR calibration system can handle these circumstances correctly, although we are not aware of any ground tests to support this. Another type of variation is caused by solar blackbody contamination, described by *Steyn-Ross et al.* [1992], *Kidwell*, [1998], *Cao et al.* [2001] and analyzed by *Trishchenko and Li* [2001]. It results from sunlight impinging on the AVHRR interior during calibration scans on certain parts of the orbit. This short-term radiative impact may last only a few minutes but can induce a significant perturbation in the
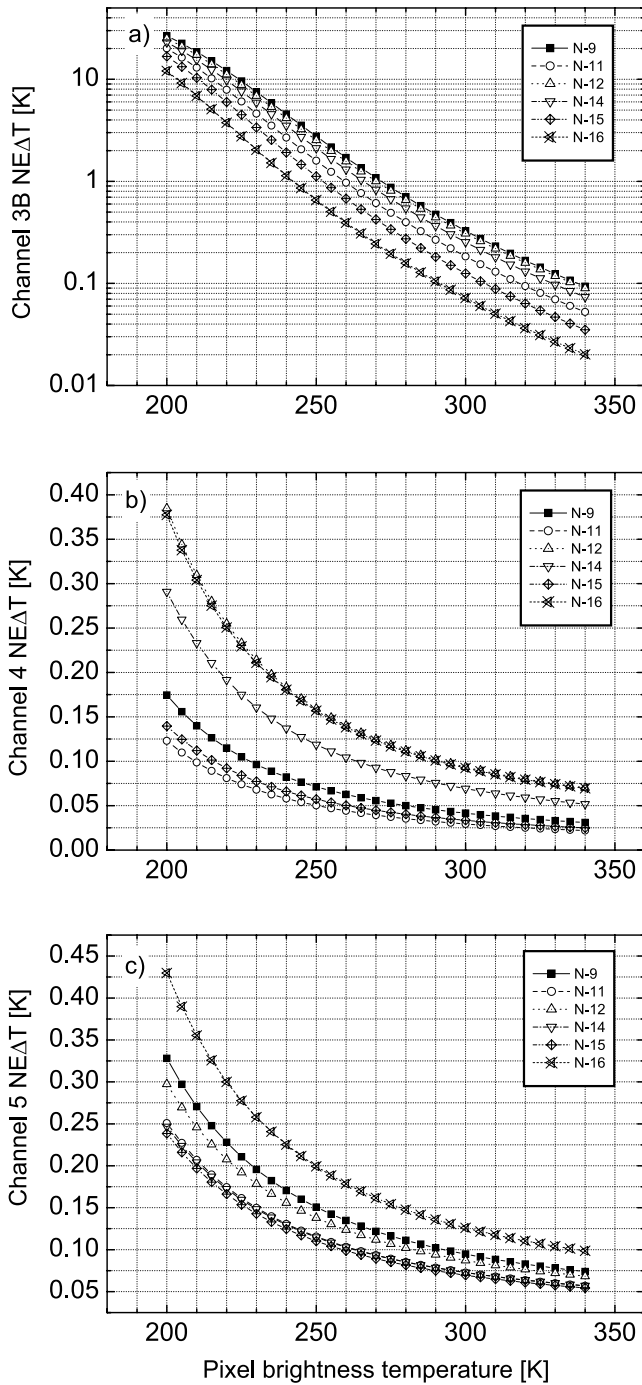
Figure 3. The NEΔT error versus pixel brightness temperature for various AVHRR radiometers computed according to equation (14) for channel (a) 3B, (b) channel 4, and (c) channel 5.

calibration data, comparable to or larger than the total range of variation during the entire orbital cycle. Therefore, a major question that has not been addressed so far is: What is the accuracy of in-flight calibration under a variable thermal environment?

[25] In principle, the calibration system is supposed to handle all possible changes in the state of an instrument. In practice, however, it is not always possible to do so. The

limiting factor seems to be the accuracy of the ICT temperature monitored by the PRTs. Figure 4 shows the variations in PRT temperatures within a single orbit for AVHHR radiometers. Each of 6 panels shows four PRT temperatures for each radiometer. An important point here is that the amplitude of ICT temperature variations within a single orbit may easily reach several degrees. The spread among temperature curves corresponding to individual PRT sensors is also quite significant. Such behavior convincingly demonstrates the existence of temperature variations and inhomogeneity of the temperature field within the ICT. The data for an individual orbit may differ from the results shown in Figure 4 in either way due to seasonal cycle and systematic orbit precession throughout of satellite lifetime, however we believe that Figure 4 gives a quite fair picture of observed perturbations.

[26] Figure 5 summarizes the variations in instrument thermal state throughout the lifetime of each instrument with four panels. The top panel (a) shows changes in average ICT temperature over the entire instrument lifetime. Long-term trends superimposed with seasonal type variations are evident. Panel (b) displays the amplitude ($\Delta T = T_{max} - T_{min}$) of ICT temperature variation within a single orbit. The ICT temperature in panel (b) is computed according to equation (3) by averaging PRT temperatures. Panels (c) and (d) show respectively the minimum and maximum spread among four PRT temperatures within a single orbit. Variations in the ICT thermal state within a single orbit may reach 7 K (AVHRR NOAA-12) as shown in panel (b). For the AVHRR/2 radiometers in general, this parameter fluctuates between 2.5 K and 7 K. For AVHRR/3 (NOAA-15, -16), the variation in the ICT temperature is smaller (1 to 3 K). This attests to the important fact that calibration of the AVHRR thermal channels takes place under nonstationary thermal conditions, with two consequences. First, the temperature of the massive calibration target (diameter ∼20 cm, *Cracknell* [1997]) cannot be monitored precisely in the presence of time-dependent thermal gradients, unless the PRTs have a very short response time to reach thermal equilibrium. Second, nonlinear relationships exist between PRT temperatures, which lead to errors in determining ICT temperatures through the linear average given by equation (3).

[27] Figure 5c indicates that AVHRR radiometers aboard NOAA-9, -15, and -16 have a small spread among PRT temperatures (typically less than 0.2 K), but the spread for others is much larger, up to 1.5 K for AVHRR NOAA-12. The difference persists over time, an indicator of possible bias in PRT calibration or persistent temperature gradients across the ICT surface. In either case, this impairs the thermal

Table 2. Estimated Average Values of the AVHRR Channel Gains Used in Computation of NEΔT

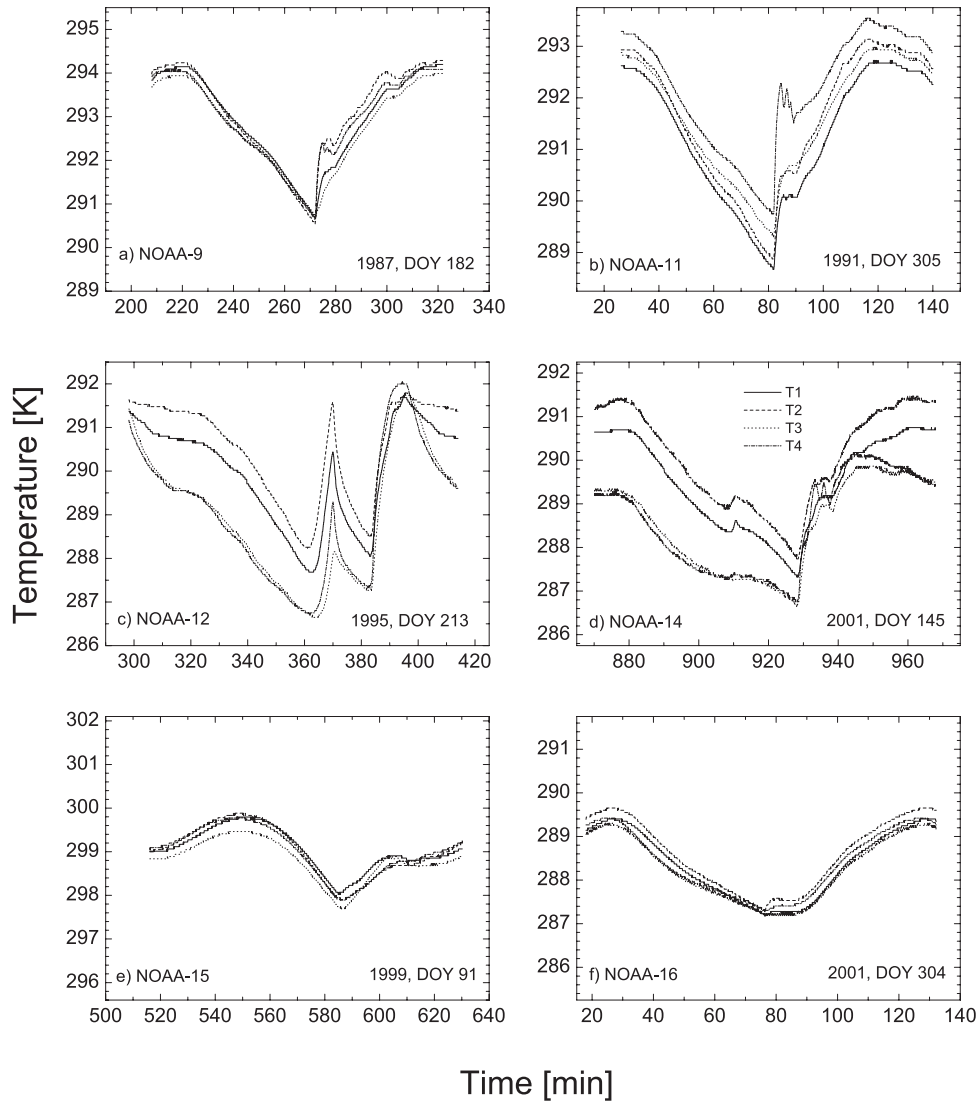| Platform	Channel 3B, mWm^{-2} str^{-1} count^{-1} cm	Channel 4, mWm^{-2} str^{-1} count^{-1} cm	Channel 5, mWm^{-2} str^{-1} count^{-1} cm
NOAA-9	−0.00145	−0.165	−0.195
NOAA-11	−0.00150	−0.175	−0.180
NOAA-12	−0.00165	−0.160	−0.180
NOAA-14	−0.00162	−0.165	−0.180
NOAA-15	−0.00240	−0.200	−0.215
NOAA-16	−0.00245	−0.185	−0.195

Figure 4. Variation in PRT temperatures for a single GAC data file. Solar contamination is observed as a sudden jump in temperature. Temperatures for individual PRT sensors are shown for (a) NOAA-9, (b) NOAA-11, (c) NOAA-12, (d) NOAA-14, (e) NOAA-15, and (f) NOAA-16. Year and day of year (DOY) are also shown.

calibration accuracy. One may consider the global minimum of the spread as an indicator of the accuracy of PRT temperature monitoring. Table 3 contains the overall minimum values and the average and median single orbit minimum spreads computed over the instrument lifetime. The analysis suggests a systematic bias of ~0.3 K in the ICT temperature determination for AVHRR aboard NOAA-11 and -14.

[28] If the temporal variations in PRT temperature are significant in a state of thermal nonequilibrium, the behavior of a detector must be described by a PRT/ICT system response time model to determine the actual temperature of the ICT. We propose to apply the following model [*Brock*, 2001]:

$$T'(t) = \frac{T_0(t) - T(t)}{\tau}, \qquad (15)$$

where $T'(t)$ is time derivative of the measured ICT temperature, $T(t)$; $T_0(t)$ is true temperature of ICT surface; τ is PRT/ICT system response time constant. t denotes time.

[29] The physical meaning of equation (15) is that the difference between sensor-reported and actual ICT temperatures is proportional to the rate of temperature change and the PRT/ICT system response time constant. This parameter characterizes the sensor's ability to respond promptly to changes in ICT temperature. Sensors with a large response time constant react slowly to temperature changes, thus introducing a delay and distortion in the temporal temperature change. To follow closely the real ICT temperature, the sensor response time must be small. Fully accurate measurements are possible only when τ is zero or at least much smaller than the perturbation period.

[30] Equation (15) provides a simple solution for the true temperature:

$$T_0(t) = T(t) + \tau T'(t). \qquad (16)$$

[31] Equation (16) includes a component proportional to the PRT response time constant and rate of temperature
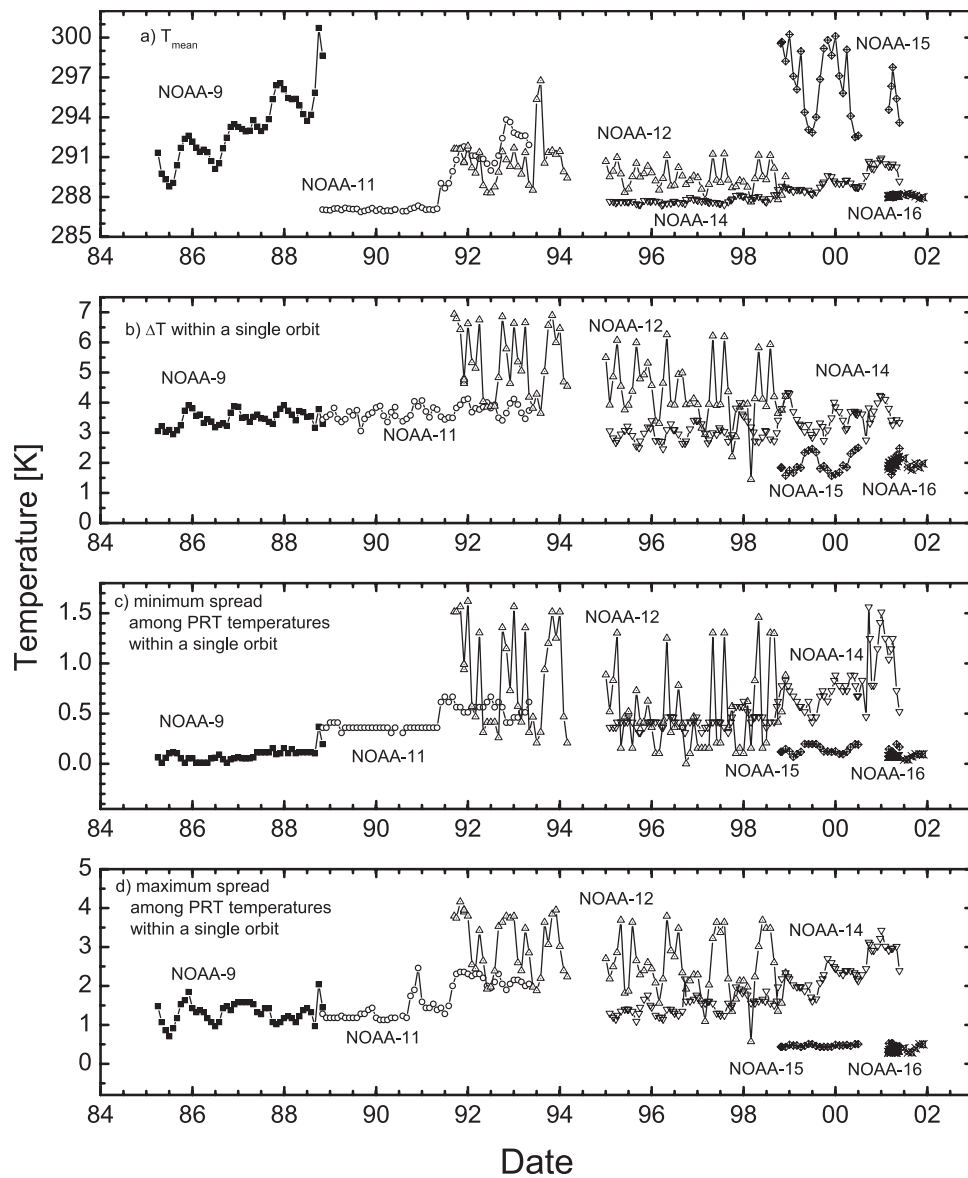
Figure 5.   Various parameters describing the ICT thermal state. (a) Single orbit average ICT temperature during the AVHRR lifetime. (b) Variation of ICT temperature within a single orbit ($\Delta T = T_{max} - T_{min}$). (c) Minimum spread among the PRT temperatures within a single orbit. (d) Maximum spread among the PRT temperatures within a single orbit.

change $T'(t)$ to characterize the sensor thermal inertia. This model is appropriate for thermal channels 4 and 5, which are not sensitive to solar radiation. The model can also be applied to channel 3B only when no solar contamination of the ICT measurements occurs. In the case of solar contamination of channel 3B, equations (15) and (16) are not applicable because they do not account for any external source of radiation, such as stray light or reflected solar radiation. A method based on Fourier transform filtering technique [*Trishchenko and Li*, 2001; *Trishchenko*, 2002] may be applied in this later case. There are indications that solar contamination may also partially affect the Earth view observations [*Kilpatrick et al.*, 2001].

[32]   To estimate the value of the PRT response time constant, we analyzed the time derivative of the ICT temperature and channel 4 and 5 gains. The results indicate

that during solar radiative contamination, channel gain and the derivative of the ICT temperature $T'(t)$ experience synchronous perturbation. Once we apply the PRT/ICT system response time model and equation (16), the spikes in the instrument gain can be eliminated by choosing an

Table 3. Statistics of Minimum Spread Between PRT Temperatures Within a Single Orbit Over the Instrument Lifetime

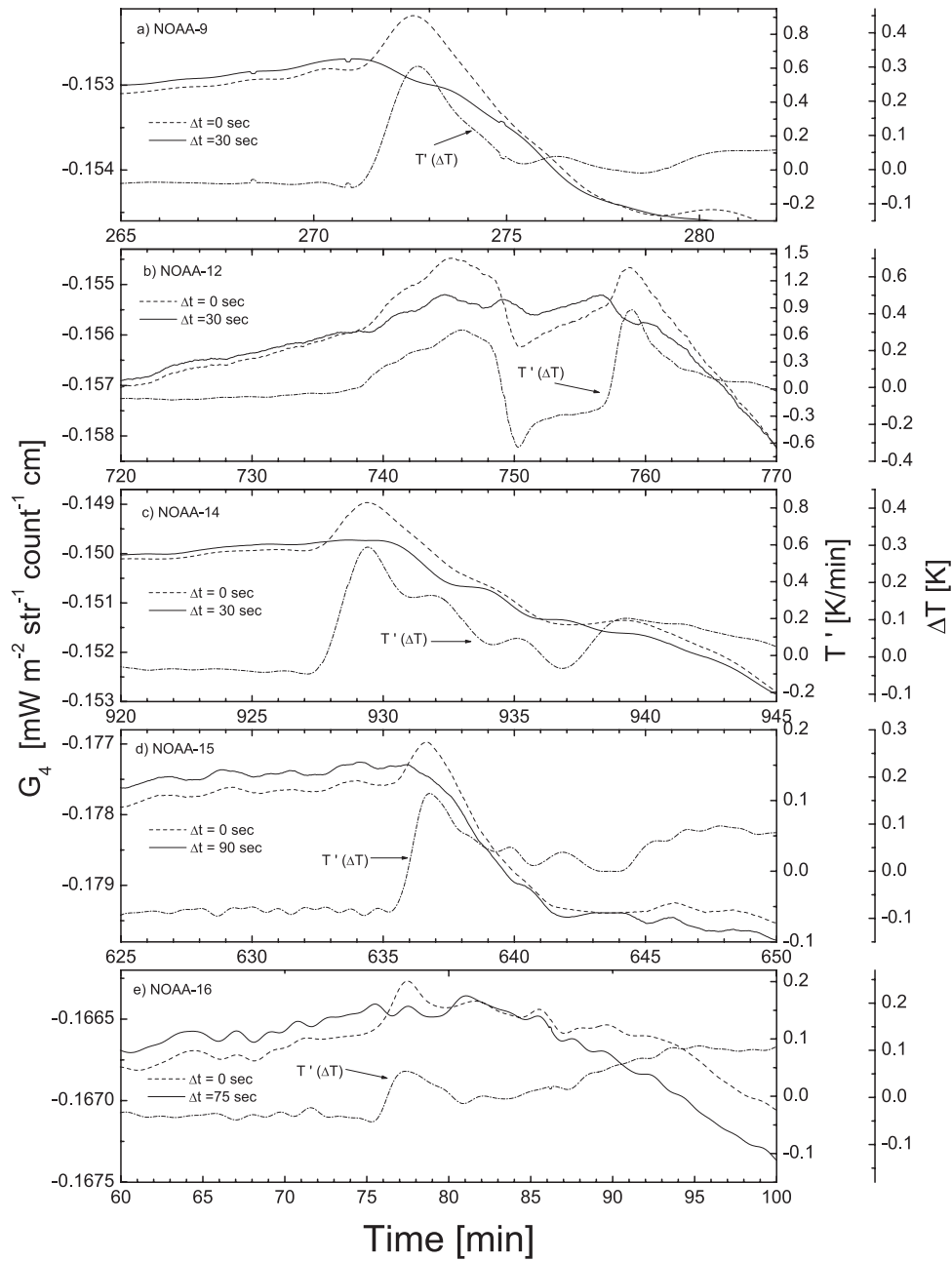| Platform	Overall minimum, K	Average Single Orbit Minimum spread, K	Median Single Orbit Minimum Spread, K
NOAA-9	0.01	0.09	0.08
NOAA-11	0.31	0.45	0.36
NOAA-12	0.10	0.67	0.49
NOAA-14	0.31	0.59	0.47
NOAA-15	0.07	0.14	0.12
NOAA-16	0.04	0.07	0.07

Figure 6. Variation in channel 4 gain G_4 and ICT temperature derivative. Uncorrected (dashed) and corrected (solid line), according to equation (16), values of gain G_4 are plotted for (a) NOAA-9, (b) NOAA-12, (c) NOAA-14, (d) NOAA-15, and (e) NOAA-16. Derivative $T'(t)$ is plotted as dash-dot line.

appropriate time constant. This is illustrated in Figure 6 for channel 4 gains. The results for channel 5 (not shown) were similar. The time constants τ were derived by computing series of instrument gain for various τ (from 5 s to 2 min) and choosing τ that removed unphysical variation of calibration gain during the period of solar contamination. Figure 6 shows panels for each AVHRR under consideration, with three curves per panel: (1) calibration gain taken from GAC data file, which was computed according to the standard definition given by equation (4); (2) time derivative of the ICT temperature determined according to equation (3); and (3) calibration gain computed with the corrected ICT temperature from equation (16). A high

degree of correlation between the original gain and the time derivative of the ICT temperature is observed. Assuming that spikes in the original gain profile are caused by thermal inertia effects described by equations (15) and (16), the PRT time response can be estimated.

[33] The values of the PRT response time constant that remove spikes in the gain profiles for a GAC orbit are $\sim$30 ($\pm$3) s for the AVHRR/2 radiometers, $\sim$90 ($\pm$9) s for AVHRR/3 NOAA-15 and $\sim$75 ($\pm$7) s AVHRR/3 NOAA-16. Values of $T'(t)$ were derived after applying Fourier transform filtering (FTF) to the ICT temperature time series to remove random noise and to apply curve smoothing necessary for numerical differentiation. The cut-off time

period in the FTF procedure was set to one minute [*Trishchenko*, 2002]. The results for all AVHRR radiometers under consideration (Figure 6) confirm that thermal inertia of PRT measurements is the major source of calibration gain perturbation. There are still some irregular variations in calibration gain after applying the correction. These may represent uncertainties arising from numerical differentiation of a discrete function and from nonlinear effects during the ICT heating/cooling, neither of which are accounted for in equation (3).

[34] Analysis of ICT temperature values indicates that the ICT temperature is monitored with an uncertainty greater than the documented NEΔT error. Two major sources of this uncertainty are the variable thermal state of the ICT, and possible inconsistencies in PRT calibration. The investigation of specific sources and quantities of errors is beyond of the scope of this study, since it cannot be based solely on available in-flight calibration measurements. The uncertainty due to the variable thermal state of the ICT includes two kinds of errors due to (1) the thermal inertia of the PRT system and (2) a nonlinear relationship between mean ICT temperature used in the calibration and the individual temperatures reported by the PRTs. The thermal inertia of the PRT/ICT system may introduce errors of ±0.5 K or more (Figure 6). A substantial spread between individual PRT temperatures (Figure 5) supports the hypothesis that a significant thermal gradient may exist across the ICT surface. The ICT used currently in the calibration of the AVHRR radiometers has a geometrical size (∼20 cm), which is close to the width of the entire AVHRR system [*Cracknell*, 1997]. The thermal state of such a massive and extended calibration target is difficult to control under nonstationary thermal conditions. This is especially true for AVHRR/2 system, where inconsistencies between PRT sensors are large. Inconsistencies between various PRTs for the AVHRR/3 system are much smaller.

5. Long-Term Trends in Thermal Calibration Coefficients

[35] Temporal variations occur in the instrument calibration gain coefficients associated with spacecraft orbital motion (Figure 4 and Figure 6). They are linked to fluctuations in the AVHRR thermal state caused by cycles of solar heating followed by thermal cooling. Temporal variations of longer periods also exist. They represent a seasonal cycle related to the change in the Sun's position relative to the spacecraft orbital plane, as well as a systematic radiometric drift (degradation) of the calibration system. The mean ICT temperatures and calibration gains fluctuate during the lifetime of an instrument (Figure 7). The average temperature per orbit is shown in Figure 7a and the calibration gains for channels 3B, 4, and 5 are shown in Figures 7b–7d, respectively. Data points in Figure 7 represent averages of a single orbit taken approximately once a month except for AVHRR/NOAA-16, where orbits were sampled more frequently because of the shorter time interval of available data. Long-term changes due to sensor degradation are evident in these panels.

[36] To separate the contribution due to seasonal temperature changes from that due to sensor degradation, we applied a two-parameter linear regression model:

$$G(T, t) = G_0 + G_T \cdot (T - T_{mean}) + G_t \cdot (t - t_0), \qquad (17)$$

where T denotes temperature and t time. The coefficient G_T determines the influence of temperature on the calibration gain, and G_t represents the level of sensor degradation with time. The estimates of the magnitude for coefficients G_T and G_t, and the r^2 statistics for the two-parameter linear regression model (equation (17)) are given in Table 4. Except for AVHRR/NOAA-9 and channel 4 of NOAA-12, the discussed regression model explains very large part of the variance, from 80% to 99%. Therefore, in general the model is indeed justified. Smaller r^2 values for NOAA-9 and ch.4 of NOAA-12 may be explained by the strongest observed solar blackbody contamination effect for these radiometers.

[37] Results presented in Table 4 show that the ICT temperature exerts a positive influence (reducing the absolute magnitude of the negative gain) on channel 3B calibration gain. With a few exceptions, the ICT temperature exerts a negative influence (increasing the magnitude of the negative gain) on channel 4 and 5 gains. Exceptions were observed for channel 5 of AVHRR/NOAA-11 and AVHRR/NOAA-14, where has small positive values of +0.01% K^{-1} and +0.11% K^{-1}, respectively. Sensor temporal changes characterized by coefficient G_t are negative for channel 3B in all AVHRR radiometers studied. They are also mostly negative for channels 4 and 5 with the exception of channel 4 of AVHRR/NOAA-9 and -16, and channel 5 of AVHRR/NOAA-15. A negative temporal trend indicates a degradation of the sensor's sensitivity with time. Except for channel 3B of AVHRR/NOAA-16, the rate of degradation is between −0.32% yr^{-1} and −0.85% yr^{-1}. The value for AVHRR/NOAA-16 (−1.4% yr^{-1}) must be interpreted with caution since it is derived from a small sample covering less than one year. While degradation of sensor sensitivity with time is quite an understandable phenomena, the temperature dependence of calibration gain reported in this paper is quite an interesting new fact, that has no trivial explanation.

[38] The calibration gain determines the scale of transformation between instrument counts and physical quantities. As such, the variation in gain affects the measurement limits. The zero radiance level is linked to the SP signal; therefore the lower observational level is always fixed. Since the observable radiance dynamic range ΔR is proportional to $G\Delta C$, where $\Delta C = 1023$ is the interval of measured counts for 10-bit data, variability in gain results in the migration of the maximum observable radiance and brightness temperature.

[39] The dynamic range of brightness temperatures that can be detected in channels 4 and 5 exceeds that observed for typical targets at the top-of-the-atmosphere (TOA) level, and consequently these channels do not reach the saturation limit. However, that is not the case for channel 3B in which both the solar reflected and thermal emitted radiation are significant. The equivalent brightness temperature of the solar constant in channel 3B is about 350 K to 360 K. As such, the sum of solar reflected and thermal emitted components may saturate the channel 3B detector. In particular, the saturation limit of channel 3B is important for remote sensing of forest fires and cloud microphysical properties. Figure 8 shows average values of maximum observable temperatures for a single orbit in channel 3B.
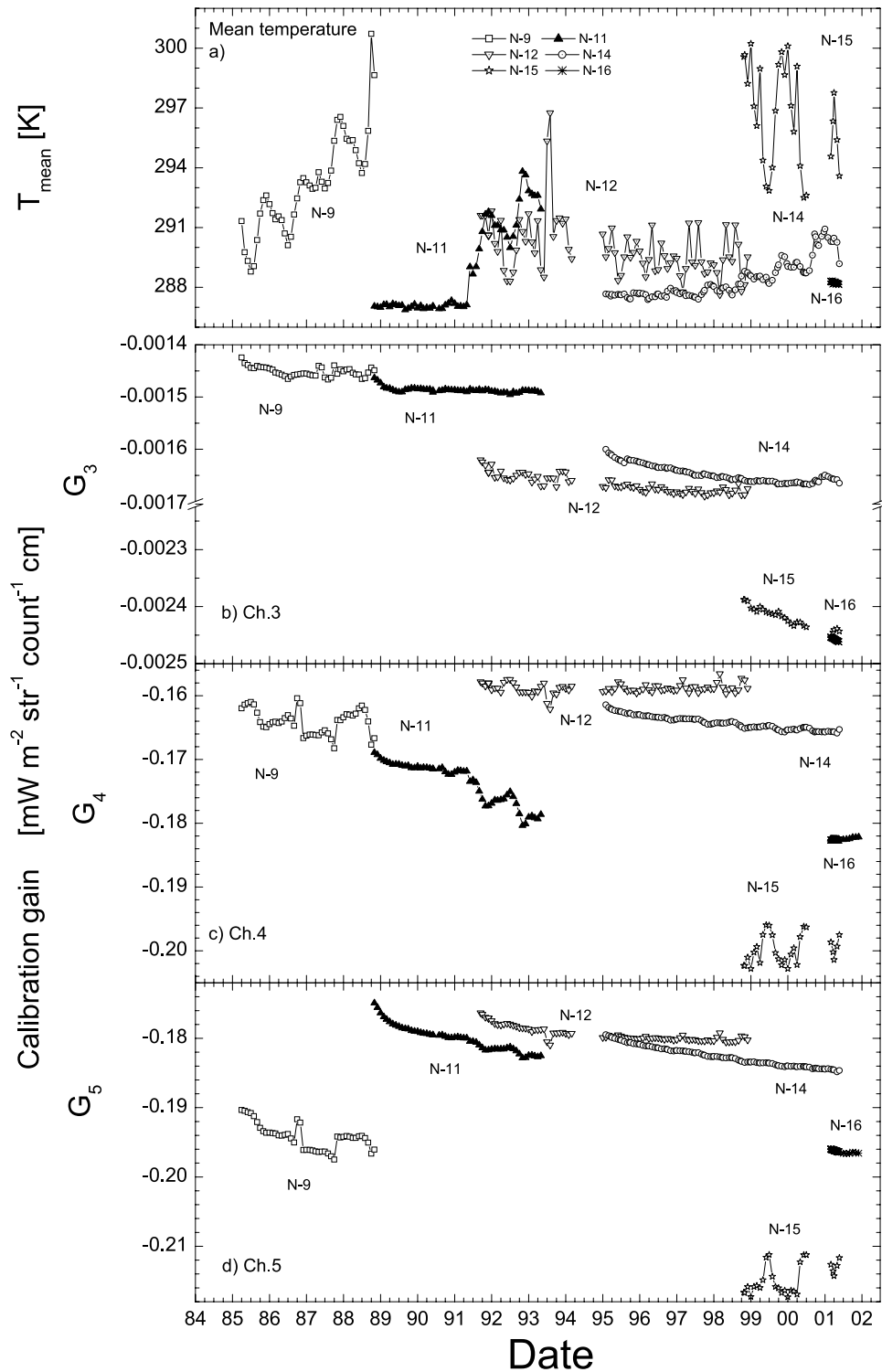
Figure 7. Long-term changes in (a) single-orbit mean ICT temperature and single-orbit mean calibration gain for NOAA-9 to -16 AVHRR channels (b) 3B, (c) 4, and (d) 5.

Upper and lower limits within a single orbit are also shown in Figure 8 as dotted curves, and the range between maximum and minimum values is marked as vertical arrows. Variations in the maximum observable temperature for AVHRR/NOAA-9, -11, and -12 within a single orbit may reach approximately ±1.5 K. This is mostly caused by solar contamination of the ICT observations in GAC data

[*Trishchenko and Li*, 2001; *Cao et al.*, 2001; *Trishchenko*, 2002]. Variations within a single orbit are significantly smaller for other radiometers (less than ±0.5 K).

[40]   The maximum observable temperature in channel 3B for AVHRR/3 (NOAA-15, -16) is significantly higher than for AVHRR/2 (NOAA-9, -11, -12, -14). It is around 336 K to 337 K for AVHHR/3 versus 321.5 K to 322.5 K for

Table 4. Coefficients of Linear Regression for the AVHRR Calibration Gains

Spacecraft	G_T, % K^{-1}	G_t, % year^{-1}	r^2
	Channel 3B		
NOAA-09	0.28	−0.81	0.49
NOAA-11	0.10	−0.32	0.48
NOAA-12	0.18	−0.34	0.81
NOAA-14	0.73	−0.81	0.92
NOAA-15	0.02	−0.85	0.92
NOAA-16	0.07	−1.49	0.99
	Channel 4		
NOAA-09	−0.35	0.38	0.23
NOAA-11	−0.57	−0.44	0.99
NOAA-12	−0.30	−0.08	0.63
NOAA-14	−0.01	−0.33	0.93
NOAA-15	−0.45	−0.17	0.98
NOAA-16	−0.34	0.17	0.81
	Channel 5		
NOAA-09	−0.04	−0.50	0.42
NOAA-11	0.01	−0.76	0.92
NOAA-12	−0.12	−0.26	0.77
NOAA-14	0.11	−0.46	0.98
NOAA-15	−0.31	0.25	0.84
NOAA-16	−0.07	−0.47	0.74

AVHRR/2. As such, the AVHRR/3 reaches saturation at higher brightness temperatures and is more suited for remote sensing studies that require wider dynamical range.

6. Summary

[41] Observations made in AVHRR thermal channels are important for weather forecasting and climate monitoring. Despite their significance and extensive applications, the accuracy of the in-flight calibration had not been rigorously investigated. This study attempted to gain insight into some particular calibration issues, including in-flight noise equivalent error (NEΔT), the consistency of PRT-based monitoring of the Internal Calibration Target (ICT) temperature, and long-term variations in calibration gains and dynamic range of the AVHRR.

[42] The study focused on the analysis of AVHRR/2 (NOAA-9, -11, -12, -14) and AVHRR/3 (NOAA-15, -16) radiometers. We utilized GAC data, approximately one orbit per month throughout the lifetime of the instruments, from the NOAA Satellite Active Archive (SAA).

[43] The overall finding of the error budget study is that AVHRR calibration measurement uncertainties are somewhat higher than assumed previously and exceed the level ±0.1 K required for climate change monitoring, even for new the AVHRR/3 (KLM series) radiometers.

[44] Analysis of the NEΔT error revealed that the threshold of 0.12 K at 300 K as stated by the instrument manufacturer was met for channels 4 and 5 most of the time; while for channel 3B of AVHRR/2 it was generally higher with a value of 0.15 K–0.3 K. The NEΔT error increases significantly at lower temperatures.

[45] Analysis of the PRT measurements uncovered complex thermal fluctuations within the ICT. PRT observations show much better consistency for the AVHRR/3 radiometer than for AVHRR/2. This finding calls for a careful reanalysis of calibration data from AVHRR/2 radiometers to produce historical thermal data sets for climate change studies.

[46] A major source of error in the calibration data is solar contamination of the ICT. The current calibration approach, as implemented in the AVHRR data processing, introduces large uncertainties (up to ±0.5 K and more) due to thermal inertia effects from rapid changes in the ICT temperature. We proposed a physical model that accounts for the thermal
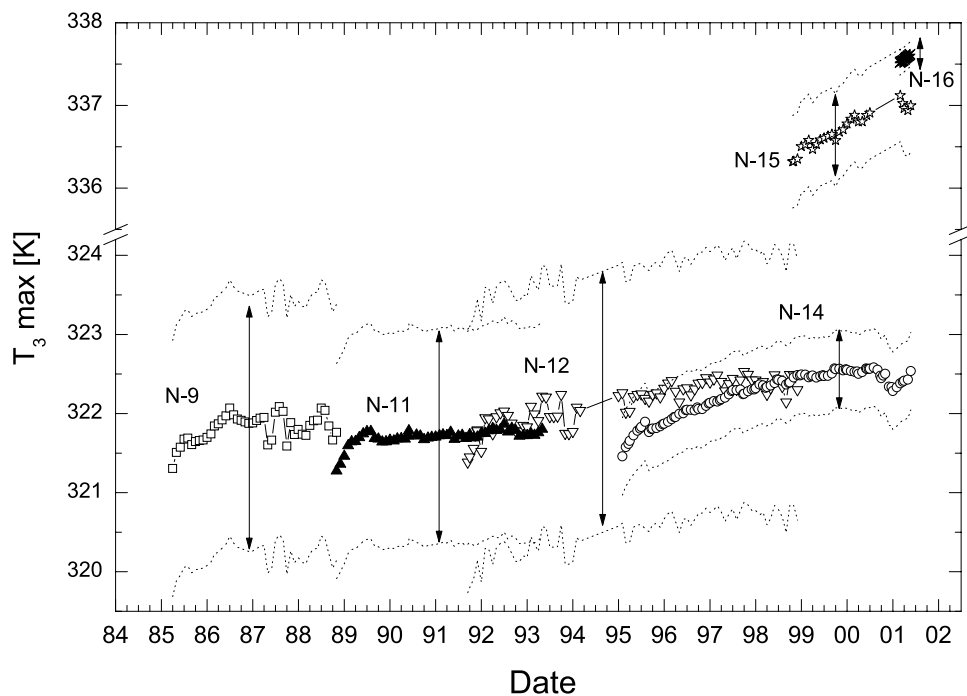

Figure 8. Maximum observable temperature in channel 3B for AVHRR/2(NOAA-9,-11,-12, and -14) and AVHRR/3 (NOAA-15 and -16) radiometers. Upper and lower dotted curves indicate a range of variation within single orbit.

inertia effect. An estimated value for the AVHRR response time constant τ is around 0.5 min for AVHRR/2 and around $1.25-1.5$ min for AVHRR/3. We estimate the uncertainty of the derived response time constant values to be between 5 and 9 s or around 10%. The model is recommended for operational use to improve thermal calibration accuracy and to better correct the influence of solar contamination. This technique also requires the implementation of a special smoothing procedure to obtain accurate results for the time derivative of ICT temperature $T'(t)$.

[47] Long-term trends in the calibration gains of IR channels 3 to 5 were evaluated. In general, a small degradation of the sensor radiometric sensitivity was detected in almost all cases, though the rate of degradation is usually quite low (typically below 0.85% year^{-1}), except for channel 3B of AVHRR/NOAA-16. Data for the latter case must be interpreted with caution due to a short observation interval. Variation in calibration gain leads to fluctuations in maximum observable target brightness temperature (upper bound of the dynamic range of temperatures that can be measured by the sensor). This is especially important for channel 3B, which may saturate during daytime and for forest fire hot spot pixels. The maximum observable temperature in channel 3B of AVHRR/2 varies between 321.5 K and 322.5 K. Newly launched radiometers show an increased maximum temperature limit of 336 K-337 K.

[48] The incorporation of the derived results and proposed improvements into AVHRR thermal calibration should result in better accuracy of derived data sets, improved consistency between various AVHRR missions, and lead to more reliable estimates of long-term changes in the Earth's climate system.

References

Brock, F. V., *Meteorological Measurement Systems*, 290 pp., Oxford Univ. Press, New York, 2001.

Brown, O. B., J. W. Brown, and R. H. Evans, Calibration of Advanced Very High Resolution Radiometer infrared observations, *J. Geophys. Res.*, 90, 11,667–11,677, 1985.

Brown, J. W., O. B. Brown, and R. H. Evans, Calibration of Advanced Very High Resolution Radiometer infrared channels: A new approach to non-linear correction, *J. Geophys. Res.*, 98, 18,257–18,268, 1993.

Cao, C., M. Weinreb, and J. Sullivan, Solar contamination effects on the infrared channels of the Advanced Very High Resolution Radiometer (AVHRR), *J. Geophys. Res.*, 106, 33,463–33,469, 2001.

Cihlar, J., Land Cover Mapping of Large Areas from Satellites: Status and Research Priorities, *Int. J. Remote Sens.*, 21, 1093–1114, 2000.

Cihlar, J., R. Latifovic, J. Chen, A. P. Trishchenko, Y. Du, G. Fedosejevs, and B. Guindon, Systematic corrections of AVHRR image composites for temporal studies, *Remote Sens. Environ.*, in press, 2002.

Cracknell, A. P., *The Advanced Very High Resolution Radiometer (AVHRR)*, 534 pp., Taylor and Francis, Philadelphia, Pa., 1997.

Goodrum, G., K. B. Kidwell, and W. Winston (Eds.), *NOAA KLM User's Guide (Revised)*, U.S. Dep. of Commer., NESDIS, NOAA, Natl. Clim. Data Cent., Satell. Data Serv. Div., Washington, D.C., 2000.

Ignatov, A., and L. Stowe, Aerosol retrievals from individual AVHRR channels, I, Retrieval algorithm and transition from Dave to 6S radiative transfer model, *J. Atmos. Sci.*, 59, 313–334, 2002a.

Ignatov, A., and L. Stowe, Aerosol retrievals from individual AVHRR channels, II, Quality control, probability distribution functions, information content, and consistency checks of retrievals, *J. Atmos. Sci.*, 59, 335–362, 2002b.

Kidwell, K. B., *Global Vegetation Index User's Guide*, U.S. Dep. of Commer., NOAA/NESDIS, Washington, D.C., 1990.

Kidwell, K. B., (Ed.), *NOAA Polar Orbiter Data User's Guide*, U.S. Dep. of Commer., NESDIS, NOAA, Natl. Clim. Data Cent., Satell. Data Serv. Div., Washington, D.C., 1998.

Kilpatrick, K. A., G. P. Podestá, and R. Evans, Overview of the NOAA/NASA advanced very high resolution radiometer Pathfinder algorithm for sea surface temperature and associated matchup database, *J. Geophys. Res.*, 106, 9179–9197, 2001.

Li, Z., L. Moreau, and J. Cihlar, Estimation of photosynthetically active radiation absorbed at the surface, *J. Geophys. Res.*, 102, 29,717–29,727, 1997.

Li, Z., Y. J. Kaufman, C. Itchoku, R. Fraser, A. P. Trishchenko, L. Giglio, J. Jin, and X. Yu, A review of AVHRR-based active fire detection algorithms: Principles, limitations, and recommendations, in *Global and Regional Vegetation Fire Monitoring from Space, Planning and Coordinated International Effort*, edited by F. Ahern, J. G. Goldammer, and C. Justice, pp. 199–225, SPB Academic Publishing, The Hague, The Netherlands, 2001.

Planet, W. G., (Ed.), Data Extraction and Calibration of TIROS-N/NOAA Radiometers, *NOAA Technical Memorandum NESS 107 Revision 1*, Natl. Oceanic and Atmos. Admin., Washington, D.C. (Amendments to NOAA Technical Memorandum 107; Appendix-B for NOAA-J/14), 130 pp., 1988.

Qin, Z., and A. Karnieli, Progress in the remote sensing of land surface temperature and ground emissivity using NOAA-AVHRR data, *Int. J. Remote Sens.*, 20, 2367–2393, 1999.

Rao, P. K., S. J. Holmes, R. K. Anderson, J. S. Winston, and P. E. Lehr (Eds.), *Weather Satellites: Systems, Data, and Environmental Applications*, Am. Meteorol. Soc., Boston, Mass., 1990.

Reynolds, R. W., and T. M. Smith, Improved global sea surface temperature analysis using optimum interpolation, *J. Clim.*, 7, 929–948, 1993.

Rossow, W. B., Measuring cloud properties from space: A review, *J. Clim.*, 2, 201–213, 1989.

Steyn-Ross, D. A., M. L. Steyn-Ross, and S. Clift, Radiance calibration of Advanced Very High Resolution Radiometer infrared channels, *J. Geophys. Res.*, 97, 5551–5568, 1992.

Stowe, L. L., A. M. Ignatov, and R. R. Singh, Development, validation, and potential enhancements to the second-generation operational aerosol product at the National Environment Satellite, Data, and Information Service of the National Oceanic and Atmospheric Administration, *J. Geophys. Res.*, 102, 16,923–16,934, 1997.

Sullivan, J., New radiance-based method for AVHRR thermal channel non-linearity corrections, *Int. J. Remote Sens.*, 20, 3493–3501, 1999.

Trishchenko, A. P., Removing unwanted fluctuations in the AVHRR thermal calibration data using robust techniques, *J. Atmos. Oceanic Technol.*, 19, 1939–1954, 2002.

Trishchenko, A. P., and Z. Li, A method for the correction of AVHRR onboard IR calibration in the event of short-term radiative contamination, *Int. J. Remote Sens.*, 22, 3619–3624, 2001.

Trishchenko, A. P., Z. Li, F.-L. Chang, and H. Barker, Cloud optical depths and TOA fluxes: Comparison between satellite and surface retrievals from multiple platforms, *Geophys. Res. Lett.*, 979–982, 2001.

Trishchenko, A. P., J. Cihlar, and Z. Li, Effects of spectral response function on the surface reflectance and NDVI measured with moderate resolution sensors, *Remote Sens. Environ.*, 81, 1–18, 2002.

Vazquez, J., and R. Sumagaysay, A comparison between sea surface temperatures as derived from the European remote sensing Along-Track Scanning Radiometer and the NOAA/NASA AVHRR ocean Pathfinder data set, *Bull. Am. Meteorol. Soc.*, 82, 925–944, 2001.

Walton, C. C., J. T. Sullivan, C. R. N. Rao, and M. P. Weinreb, Corrections for detector nonlinearities and calibration inconsistencies of the infrared channels of the Advanced Very High Resolution Radiometer, *J. Geophys. Res.*, 103, 3323–3337, 1998.

————————

J. Cihlar, G. Fedosejevs, and A. P. Trishchenko, Canada Centre for Remote Sensing, Natural Resources Canada, 588 Booth Street, Ottawa, Ontario, K1A 0Y7 Canada. (josef.cihlar@ccrs.nrcan.gc.ca; gunar.fedosejevs@ccrs.nrcan.gc.ca; trichtch@ccrs.nrcan.gc.ca)

Z. Li, ESSIC, University of Maryland, 2335 CSS Building, College Park, MD 20742, USA. (zli@atmos.umd.edu)